Formation and evolution of sediment layers in an aggregating colloidal suspension

Myung Han Lee and Eric M. Furst*

Department of Chemical Engineering, University of Delaware, Colburn Laboratory, 150 Academy Street, Newark, Delaware 19716, USA

(Received 23 February 2006; revised manuscript received 30 May 2006; published 7 September 2006)

The coupled aggregation and sedimentation of colloidal particles with short-range attractions are investigated. Nonadsorbing polymer is used to induce depletion interactions between the hard-sphere particles. Gravitational forces, caused by a density mismatch between the particles and the suspending fluid, result in the sedimentation of particles and aggregates, as well as the compaction and rearrangement of the final sediment layer. At low polymer concentrations C_P, or low initial volume fractions ϕ_o, clusters formed during the period of fast sedimentation are small, and the structure of the final sediment is dense. Conversely, at high C_P, or high ϕ_o, large clusters form during sedimentation, and the resulting sediment structure is significantly less dense, with large void volumes. The size of the presediment aggregates depends on C_P and ϕ_o with a functional form that resembles other thermally activated barrier hopping processes in colloidal systems, such as the delayed sedimentation of colloidal gels. Finally, when the particles are weakly attractive, gravitational stresses are found to induce compaction of the sediment over long periods of time. However, sediments composed of particles that are strongly attractive resist rearrangements and compaction, even when the sediment layers have a relatively large amount of free volume.

DOI: 10.1103/PhysRevE.74.031401 PACS number(s): 82.70.Gg, 61.20.Lc, 82.70.Dd, 61.43.Hv

I. INTRODUCTION

Particle aggregation is of great interest not only due to the variety of roles it plays in biological systems, medical diagnostics, paints and coatings, and numerous foods but also as a model system for growth under nonequilibrium conditions [1–3]. In the past two decades, work has focused on the formation of aggregates, including their geometry and growth kinetics, in the absence of sedimentation [4–9]. Strong attractive interparticle interactions cause dispersed colloidal suspensions to form fractal-like aggregates of k particles with radius of gyration $\xi \approx ak^{1/D_f}$, where D_f is the fractal dimension [10,11]. The aggregate fractal dimension and ultimate gel structure depend on the kinetics of aggregation. Typically, clusters exhibit a range from $D_f=1.8$ for diffusion-limited cluster aggregation (DLCA) to 2.1 for reaction-limited growth (RLCA) [5,12]. When the volume fraction of the particles within the floc, ϕ_k, equals the initial bulk volume fraction of suspension, a sample-spanning network is formed, signifying the onset of gelation [13]. However, many real aggregation phenomena rarely take place under quiescent conditions but instead occur in the presence of gravitational fields or macroscopic flows. In addition, external fields, including electrical, magnetic, and optical, have proven useful for assembling colloidal systems, such as colloidal crystals [14–17]. Therefore, the combined action of aggregation and sedimentation has drawn increasing attention in recent years [18–21].

It is known that sedimentation affects the kinetics of growth and structural properties of colloidal gels. For instance, Manley and co-workers found that gravitational forces limit cluster growth, constraining the gel formation [22]. As a result, the time evolution of cluster size in the presence of gravity significantly deviates from DLCA behavior. Allain and co-workers also examined the settling behavior in colloidal suspensions in the presence of attractive forces between particles [20]. They found that the critical gel concentration ϕ^* increases remarkably in a gravitational field. They also reported the increase in the fractal dimension of settling clusters due to flow-induced restructuring. Moreover, after a gel forms, gravitational forces result in the breakup and compression of the structure, and stresses induced by sedimenting dense fractions cause restructuring of less dense ones. Starrs and coworkers reported that in Poly(methylmethacrylate)-poly(styrene) (PMMA-PS) mixtures the time evolution of height of the sediment shows an unexpected scaling behavior, suggesting a universal nature to this delayed collapse [23]. Manley and co-workers also studied the gravitational collapse of colloidal gels [24]. They found that the collapse of gels is determined by a balance between the gravitational stress, the resistance to fluid flow, and their elastic and plastic properties. Clearly, knowledge of colloidal aggregation and rearrangements under the influence of gravity will ultimately provide a thorough understanding of the processes occurring in real aggregating systems, and will also serve as an useful model for aggregation and rearrangements in a variety of external fields.

In this study, we investigate the coupling between the aggregation and sedimentation of colloid particles as functions of the strength of attraction and initial particle volume fraction, using confocal microscopy, in the initial, intermediate, and final stages of structural development. The strength of attraction between particles is controlled by the concentration of a nonadsorbing polymer. Using this approach, we relate the final sediment structure and compaction properties to the aggregation behavior of the presediment.

The remainder of this paper is divided into three sections. First, we detail the experimental approach, including the synthesis of core-shell silica particles using a modified Stöber synthesis. We then present the significant results, focusing on the kinetics of growth prior to the formation of the sediment layer, the structural characteristics of the sediment, and the

*Corresponding author. E-mail: furst@che.udel.edu

longtime compaction processes that occur in dense layers. In the discussion, we detail the connection between these processes as they relate to the kinetics of bond formation and breakage in attractive colloidal systems. We conclude with final remarks and possible directions for future work.

II. EXPERIMENTAL

A. Synthesis of fluorescent core-shell silica particles

The fluorescent core-shell silica particles used for this study are synthesized using a modified Stöber method, as described previously [25]. Core-shell particles allow for imaging individual particles inside a dense colloidal suspension, and prevent dye molecules from affecting the particle interactions. The particle synthesis is briefly described below.

The fluorescent dye, fluorescein isothiocyanate (FITC, isomer I), is covalently attached to the silane coupling agent, (3-aminopropyl)triethoxysilane (APS), by mixing APS (20 mM) and FITC (5 mM) in 5 ml of ethanol for 15 h. Then, two types of ethanol solutions with identical volumes, denoted as solution I and solution II, are prepared separately. Solution I consists of NH_4OH (1.0 M NH_3), sodium dodecyl sulfate (10.4 mM; SDS), and H_2O. Solution II contains tetraethyl orthosilicate (0.4 M; TEOS) and the product of APS and dye FITC. These solutions are mixed together with continuous stirring for 6 h. The H_2O/TEOS molar ratio (R_w) is fixed at 50. After the reaction, the samples are washed with ethanol by centrifugation and decantation several times in order to remove unreacted chemicals. A seeded growth technique is then used to synthesize a nonfluorescent silica shell on the fluorescent silica spheres. The particles are dispersed in ethanol containing NH_4OH (0.50 M) and H_2O (7.80 M). TEOS (0.12 M) is added continuously in a semibatch operation to minimize the potential for secondary nucleation. The diameter of the final core-shell particles, measured using transmission electron microscopy (TEM), is 1.454 ± 0.048 μm. They include few percent of doublets and triplets.

The density of silica particles ($\rho = 2.024$ g/cm^3) is determined using density mixing equation

$$\frac{1}{\rho_{mix}} = \frac{1}{\rho_{ETOH}} x_{ETOH} + \frac{1}{\rho_{Silica}} x_{Silica}, \tag{1}$$

where x_i is the weight fraction of species i when the core-shell silica is dispersed in pure ethanol. The suspension density data at dilute concentrations is obtained using a commercial densiometer (Anton Paar DMA 48), as shown in Fig. 1. The particle volume fraction is calculated by drying and weighing a known amount of silica particles.

B. Sample preparation

The silica particles are dispersed in refractive index matched solvent, tetrahydrofurfuryl alcohol (THFA; $n = 1.452$, $\rho = 1.054$ g/cm^3). Short-range attraction is induced through the addition of nonadsorbing polystyrene (PS, $M_w = 110\,000$) with $r_g = 10.3$ nm and $\xi = r_g/a \approx 0.014$. The

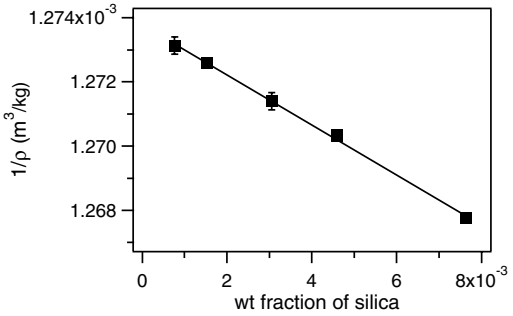

FIG. 1. Density profile of silica solutions at dilute concentrations, fitted with the density mixing equation [Eq. (1)].

colloid-polymer solutions are prepared by mixing two stock liquids: (I) a silica dispersion in THFA; (II) a polystyrene solution in THFA. Each solution is prepared by adding silica or polystyrene to THFA solvent and dispersing them using a vortex mixer and sonicator for 1 h. Next, these solutions are mixed together using a vortex mixer. We determine the adding polymer concentrations through the magnitude of depletion-induced attraction. The lowest polymer concentrations used (2.8 and 4.1 mg/ml) correspond to magnitudes of the depletion attraction at contact of -8 and $-12kT$, respectively. The lowest polymer concentration is chosen by the critical polymer concentration for gelation proposed by Tolpekin and co-workers [26]. They studied the aggregation and breakup of silica particles in shear flow, using confocal microscopy, using a dispersion medium that met the requirements of close refractive index and density matching. They found that the critical concentration for gelation is between 1.8 and 2.2 g/L of poly(ethylene glycol) (PEG), corresponding to $U \sim -8$ kT. In our system, however, gelation in the bulk does not occur under any of conditions tested due to the rapid sedimentation caused by gravity [20,22]. Therefore, all experiments are considered to be in the regime of cluster deposition in the absence of gelation.

The sample cells are composed of a #1 cover glass glued to a glass microscope slide. Glass spacers are used to construct a 0.2 mm gap. The sample area is approximately 10×20 mm^2. The colloid-polymer solution is injected into the cell and carefully sealed with epoxy to prevent solvent evaporation and photobleaching of the fluorescent particles. The samples are relatively small, and because the material is loaded with capillary action, we expect that any macroscopic flow not driven by the sedimentation decays rapidly. When the sample is drawn in, shearing can cause significant aggregation and compaction. Therefore, we take care to redisperse the particles by pressing vigorously on the cover slip and repeatedly flipping the cell before taking images. This provides consistent results. The starting time of aggregation is taken after this resdispersion step.

In our system, the gravitational Peclet number (Pe_g), given by

$$\mathrm{Pe}_g = \frac{t_B}{t_g} = \frac{4\pi\Delta\rho a^4 g}{3k_B T} \tag{2}$$

is 2.7, where t_B is the characteristic diffusion time and t_g is the settling time. With Pe_g, we can identify the relative im-

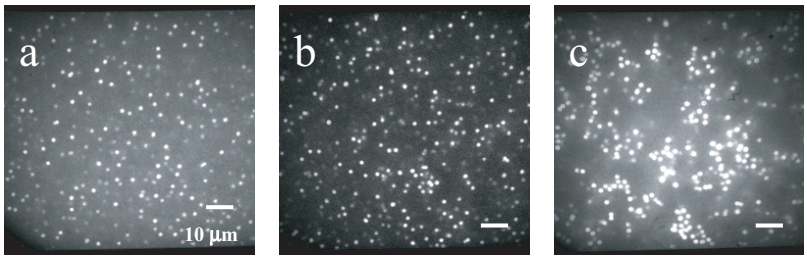

FIG. 2. Confocal images of the presediment structure at $\phi_o=0.052$ as a function of C_P: (a) 0 mg/ml, (b) 8 mg/ml, and (c) 15 mg/ml.

portance of settling over diffusion. For instance, if $Pe_g \ll 1$, then Brownian motion determines the rate of collision of the particles, whereas if $Pe_g \gg 1$, sedimentation prevails over Brownian motion. In a mixed system of colloid and polymer with high $Pe_g(>1)$, particle aggregation is considerably influenced by sedimentation.

C. Confocal microscopy

The microstructure of mixtures of silica and PS polymer in THFA is imaged with confocal microscopy. A Nipkow confocal (Yokogawa Electric. Co., model CSU10) used in our study differs from common scanning confocal microscope, because it utilizes a multipinhole spinning disk. Thus, the pinhole coverage of the focal plane is completed several hundred times per second, effectively creating a full confocal image in real time. Using a 63× oil-immersion objective, the aggregation and sedimentation of silica particles in polymer solutions are visualized directly. Images are captured using a 10-bit intensified charge-coupled device (CCD) camera (Stanford Photonics XR-MEGA/10), and stored on a hard drive for later processing.

The microstructure is characterized from confocal images at early and late time points in the evolution of the aggregating suspension. The sedimenting suspension forms a quiescent structure within approximately 20 min, which is governed by the sedimentation rate. For single particles, the sedimentation rate is approximately 0.18 μm/s, which means that single particles at the top of the sample will deposit in a layer at the bottom within roughly 18 min. Large clusters, such as doublets and triplets, settle faster than single particles, so this represents a maximum time of sedimentation. After the sediment forms, the suspension structure evolves slowly enough that three-dimensional (3D) image volumes can be obtained. These are reconstructed by collecting two-dimensional (2D) image slices using a piezo objective positioner (Physik Instrumente, model P-721.CDQ). Image processing is carried out on the image volumes to generate the 3D particle positions, using a modified version of the particle tracking algorithms described by Crocker and Grier [27] and Varadan and Solomon [28]. We estimate that the image acquisition error of the particle positions is less than 30 nm in the xy direction and 25 nm in z direction due to subvoxel accuracy.

III. RESULTS

A. Presediment structure

Images of the suspension early in the aggregation process are taken at a fixed position 10 μm above the container bottom while varying the polymer concentration and initial particle volume fraction. The images are taken approximately 1 min after the redispersion step, described in Sec. II B. Examples for $\phi_o=0.052$ are shown for various polymer concentrations in Fig. 2. In the absence of polymer, the particles are uniformly distributed, as expected. As the polymer concentration increases, particles form small clusters such as doublets and triplets in the suspension, as shown in Fig. 2(b) for $C_P=8$ mg/ml. At the higher polymer concentrations, large clusters and transient percolating structures form rapidly due to the large attractive well depth. As we discuss below, this early aggregation behavior during sedimentation has a profound influence on the ultimate structure of the sediment and the longtime compaction characteristics.

The nature of the growing structure depends both on the collision frequency of particles and aggregates and the sticking probability, or the likelihood that particles in contact remain bound together. Confocal images, such as those shown in Fig. 2 are analyzed quantitatively by measuring the average cluster size $\langle \xi \rangle_m$. The average cluster size is calculated by first dilating the particle sizes within the image to compensate for the nonfluorescent shell, and then thresholding the image to identify the individual flocs. The structure formed at high C_P, or high ϕ_o, exhibits the broad size distribution, including many singlets and doublets that skew the number-averaged cluster size. Instead, we calculate the two-dimensional mass average cluster size

$$\langle \xi \rangle_m = \frac{\sum_{i=1}^{n} w_i \xi_i}{\sum_{i=1}^{n} w_i}, \tag{3}$$

where n is the total number of flocs, $w_i=(\xi_i^2/a^2)$ and a is the single particle radius. Each mass average cluster size calculated consists of an average of floc radius over on the order of 100 aggregates. To characterize each cluster by its two-dimensional size, we assume that the aggregates are relatively isotropic. Earlier, González and co-workers demonstrated using computer simulations that the elongation of clusters along the vertical direction occurs for high Peclet numbers ($Pe_g=0.1$ and 1), when the clusters are nonrotating [29]. This was explained by a mechanism in which larger clusters, which move faster, sweep the particles below. By observation of aggregates moving through the imaging plane, we find that flocs appear to rotate sufficiently such that their structures are not highly anisotropic.

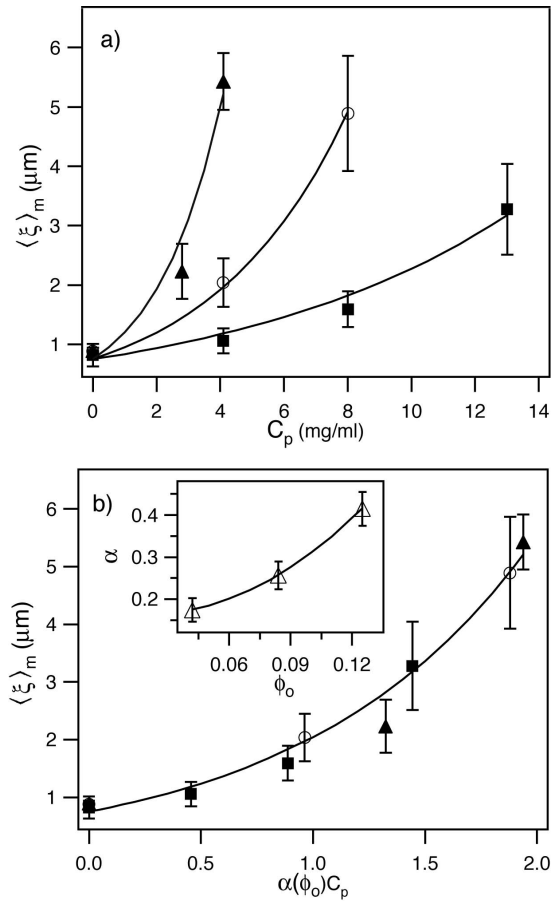

FIG. 3. Average cluster size of the presediment microstructure for different volume fractions: (■) ϕ_o=0.042; (○) ϕ_o=0.084; (▲) ϕ_o=0.125. Average cluster sizes are plotted as a function of (a) C_P and (b) $\alpha(\phi_o)C_P$. The inset shows the fitting parameter, α, versus particle volume fraction, ϕ_o.

Figure 3(a) shows the average cluster radius, $\langle \xi \rangle_m$, approximately 1 min after inducing aggregation. $\langle \xi \rangle_m$ increases with increasing C_P and ϕ_o. For instance, at ϕ_o=0.042, large clusters do not form until C_P approaches 12 mg/ml; at lower concentrations of nonadsorbing polymer, only single particles and small clusters are found. In contrast, at ϕ_o =0.125, the cluster size at short times increases rapidly with C_P, and particle aggregates with $\langle \xi \rangle_m$=5.5 μm are observed at C_P=4.1 mg/ml. We find that for each ϕ_o, $\langle \xi \rangle_m$ depends exponentially on polymer concentration,

TABLE I. Sediment packing fraction analysis. The sediment volume fractions are calculated by counting particles in volumes of $40\times40\times10$ μm^3. The asterisks indicate significantly lower sediment volume fractions that define a critical polymer concentration C_{crit}.

ϕ_o	C_P (mg/ml)	Sediment volume fraction (ϕ_{sed}) 20 min	60 min	100 min
0.042	0.0	0.517	0.563	-
	4.1	0.467	0.504	-
	8.0	0.425	0.436	-
	13.0*	0.341	0.351	0.359
0.084	0.0	0.546	0.575	-
	4.1	0.508	0.535	-
	8.0*	0.336	0.348	0.352
0.125	0.0	0.555	0.618	-
	2.8	0.497	0.532	-
	4.1*	0.256	0.263	0.294
	8.0*	0.273	0.282	0.283

$$\langle \xi \rangle_m = a \exp(\alpha C_P). \quad (4)$$

The fitting parameter α is a function of ϕ_o, as shown in the inset of Fig. 3(b). The parameter α is empirically found to be a polynomial function of volume fraction,

$$\alpha(\phi_o) = 34.37\phi_o^2 - 1.38\phi_o + 0.11. \quad (5)$$

Based on Eqs. (4) and (5), the average cluster size, $\langle \xi \rangle_m$ for each initial volume fraction collapses as a function of $\alpha(\phi_o)C_P$, as shown in Fig. 3(b). Equation (4) resembles the form found in other activated barrier hopping processes in colloidal systems, and highlights the influence of the sticking probability on aggregate growth in a gravitational field. The significance of Eqs. (4) and (5) is discussed in more detail below.

B. Sediment structure

As mentioned above, the sedimenting suspension forms a quiescent structure within a maximum time of approximately 20 min. Figure 4 shows images of the structure as a function of polymer concentration at a fixed initial volume fraction ϕ_o=0.042. The volume fractions of the sediment ϕ_{sed} are calculated from 3D confocal images, and are summarized in

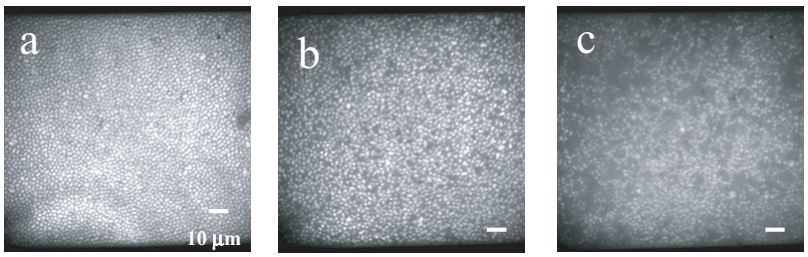

FIG. 4. Confocal images of the structure of the sediments formed at ϕ_o=0.042 as a function of C_P: (a) 0 mg/ml, (b) 8 mg/ml, and (c) 13 mg/ml.

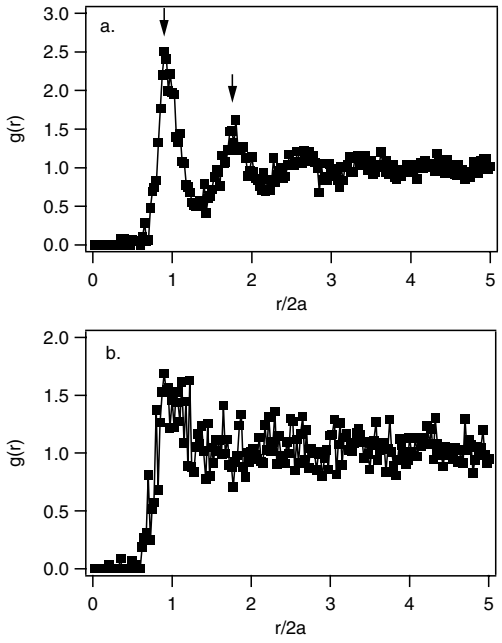

FIG. 5. Radial distribution functions of the sediments formed at ϕ_o=0.042 as a function of C_P: (a) 0 mg/ml, (b) 13 mg/ml. The arrows indicate expected peaks for hexagonal packing.

Table I. At C_P=0, the sediment visually appears to be partially crystalline, with ϕ_{sed}=0.517. The microstructure is characterized by calculating the radial distribution function, $g(r)$, which describes the probability of finding a pair of particles a distance r apart, relative to the probability expected for a completely random distribution at the same density. In the absence of polymer, the radial distribution function [Fig. 5(a)] shows several sharp peaks. The first and second peaks at $2a$ and $2\sqrt{3}a$ are expected for a hexagonal close-packed configuration. This confirms that the sediment is at least partially ordered, rather than an amorphous solid. At C_P=8 mg/ml, the sediment is dense, with ϕ_{sed}=0.425, while for C_P=13 mg/ml, the volume fraction of sediment is significantly lower, with ϕ_{sed}=0.341, and there are many voids in the structure. In the presence of polymer, the radial distribution function [Fig. 5(b)] for the sediments does not exhibit specific peaks, indicating a disordered sediment. The sediment structures at other values of ϕ_o exhibit similar trends as those in Figs. 4 and 5, including a critical polymer concentration C_{crit}, which marks a transition to sediments with significantly lower volume fractions. For instance, Table I shows that sediments formed at C_P=8 mg/ml for ϕ_o =0.084 and $C_P \geq 4.1$ mg/ml for ϕ_o=0.125 exhibit ϕ_{sed} between 0.26 and 0.34, compared with $\phi_{sed} \approx 0.50$ at lower polymer concentrations.

As mentioned earlier, the microstructure of colloidal gels is typically characterized by the fractal dimension, D_f. This is commonly calculated from the suspension structure factor $S(q) \sim q^{-D_f}$ measured with scattering experiments, where q is the scattering wave vector [5,30]. Alternatively, one can calculate D_f in microscopy experiments from particle positions using the integrated pair correlation function [31]

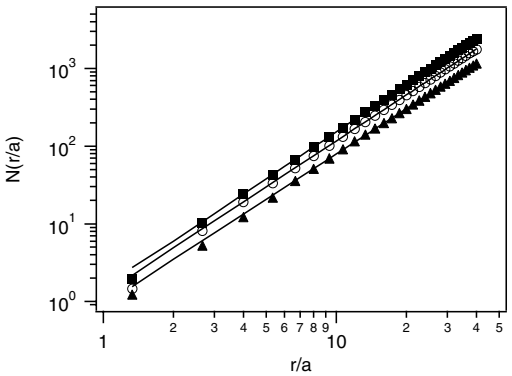

FIG. 6. The integrated pair distribution function $N(r/a)$ as a function of C_P for ϕ_o=0.042: (■) 0 mg/ml; (○) 8 mg/ml; (▲) 13 mg/ml. The slope of $N(r/a)$ is the fractal dimension D_f.

$$N(r) = 4\pi \int_0^r s^2 g(s) ds = N_0 \left(\frac{r}{a}\right)^{D_f}. \quad (6)$$

Over large distances, the characterization of the structure is limited by the depth of the z direction in the 3D confocal images; therefore, we use 2D confocal slices. We calculate D_f from a modified form of Eq. (6),

$$N(r/a) = N_0 \frac{\Delta z}{a} \frac{D_f}{D_f - 1} \left(\frac{r}{a}\right)^{D_f - 1}, \quad (7)$$

which provides information about the 3D structure from 2D confocal slices with thickness Δz [26]. In Fig. 6, we plot $N(r/a)$ for ϕ_o=0.042 and C_P=0, 8, and 13 mg/ml. Fractal dimensions, D_f, are calculated by fitting the data to Eq. (7), and are summarized in Table II for all experimental conditions. At an initial volume fraction of ϕ_o=0.042, stronger attractions at higher polymer concentrations lead to lower particle density due to many voids in the sediment, as shown by the decreasing magnitude of $N(r/a)$ in Fig. 6. However, the fractal dimensions of the sediments do not change significantly, and exhibit only a slight decrease in D_f (Table II). The values ($2.9 < D_f \leq 3.0$) correspond to dense structures

TABLE II. Fractal dimension, D_f, of sediments as functions of ϕ_o and C_P.

ϕ_o	C_P (mg/ml)	Fractal dimension (D_f)
0.042	0.0	2.998±0.003
	8.0	2.989±0.004
	13.0	2.921±0.010
0.084	0.0	3.001±0.001
	4.1	2.995±0.002
	8.0	2.957±0.006
0.125	0.0	3.001±0.002
	2.8	2.997±0.002
	4.1	2.956±0.002
	8.0	2.906±0.003

that do not exhibit structural self-similarity. This distinct difference from DLCA (D_f=1.75) and RLCA (D_f=2.0~2.2) structures can be partially explained by the high density of the sediment. Earlier experiments and simulations found that high particle concentrations lead to nonfractal structures [32–34]. For instance, van Garderen and co-workers observed the influence of the concentration on the fractal dimensions in three dimensions using computer simulations [34]. The increase of particle concentrations from 0.25 to 30%, causes an increase in D_f from approximately 1.74 to 3.0. A second contributing factor is the degree of restructuring and rearrangments that are likely to occur as the aggregates sediment.

The number density fluctuation $(\langle N^2\rangle - \langle N\rangle^2)/\langle N\rangle$ provides an alternate means for evaluating the sediment structure [35]. The density fluctuations are calculated by dividing 3D confocal images into smaller subvolumes of dimension L and counting the number of particles in each subvolume. The number density fluctuation is related to the low scattering vector limit of the structure vector and the gel isothermal compressibility χ_T [35,36],

$$S(q \to 0) = \lim_{a/L \to 0} \frac{\langle N^2\rangle - \langle N\rangle^2}{\langle N\rangle} = \rho k_B T \chi_T. \tag{8}$$

In our study, L is limited to 10 μm due to the smallest dimension of the confocal volume ($40\times40\times10$ μm^3).

Figure 7 shows the number density fluctuations for each initial volume fraction. At C_P=0 mg/ml and ϕ_0=0.042, the density fluctuations decrease slightly and then reach a plateau as with increasing L, corresponding to the even distribution of particles throughout the volume, as shown in the confocal images (Fig. 4). The curve for C_P=4.1 mg/ml follows the trend of the polymer-free case, but is shifted up slightly. In the presence of larger attractive interactions, on the other hand, density fluctuations follow the C_P =0 mg/ml curve at low values of L, then increase as L increases further. The point at which the curves deviate provides a characteristic length scale over which the compact structure begins to exhibit greater porosity. For C_P $\geqslant$8.0 mg/ml, this occurs at approximately a/L=0.19–0.22, corresponding to lengths on the order of 5 particle radii. At higher ϕ_0 [cf. Fig. 7(c)], $a/L\sim0.3$, indicating that the density is significantly lower. It is interesting to note that these length scales are significantly outside the range of even ultrasmall angle x-ray scattering (USAXS) and ultrasmall angle neutron scattering (USANS) measurements [37].

C. Sediment compaction

After the initial aggregation process has ended, the resulting sediment is largely quiescent, but exhibits slow compaction. In the silica suspensions investigated here, the initial sediment volume fraction varies over a substantial range, from ϕ_{sed}=0.25 to 0.56, depending on the polymer concentration and particle volume fraction (cf. Table I.) As discussed above, the initial sediment structure is largely due to the competition between aggregation and sedimentation. We find that further compaction of the structure depends primarily on C_P, which governs the strength of attraction between

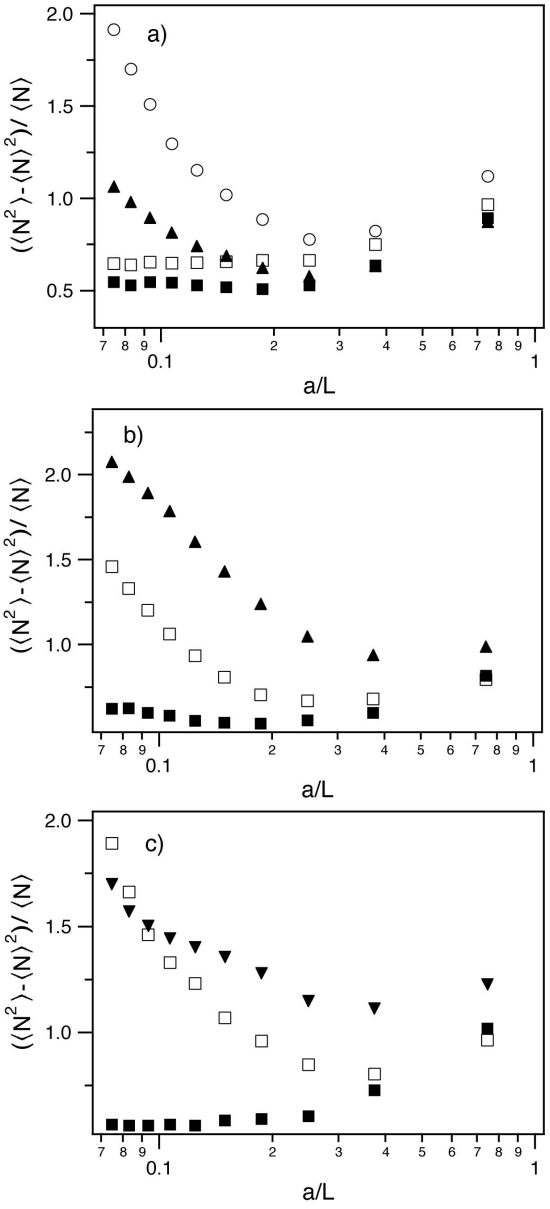

FIG. 7. The number density fluctuation $(\langle N^2\rangle - \langle N\rangle^2)/\langle N\rangle$ as a function of subvolume size L for (a) ϕ_o=0.042; (b) ϕ_o=0.084; (c) ϕ_o=0.125: (■) C_P=0 mg/ml; (▽) C_P=2.8 mg/ml; (□) C_P =4.1 mg/ml; (▲) C_P=8 mg/ml; (○) C_P=13 mg/ml.

particles. In the absence of nonadsorbing polymer at each initial volume fraction investigated, compaction of the sediment leads to the formation of a glassy, partially crystalline structure. Sediments formed at low polymer concentrations ($C_P \leqslant 4.1$ mg/ml), exhibit more compaction than those at higher polymer concentrations ($C_P \geqslant 8.0$ mg/ml). Table I shows that sediments bound by weakly attractive interactions increase in volume fraction by 5–10% over a 1 h period, while the increase in ϕ_{sed} is on average 2–3% for more strongly attractive samples.

To characterize the compaction process further, we determine changes in the number of nearest neighbors in contact, or bond number N_b, for each particle in the sediment. N_b is determined by measuring the center-to-center separation be-

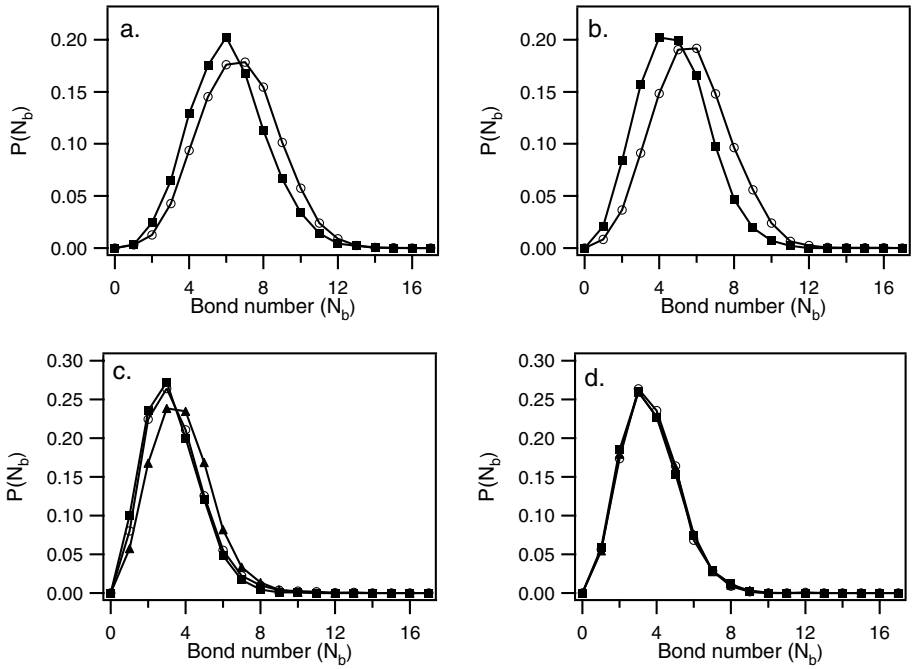

FIG. 8. Distribution of the number of bonds per particle, N_b, at $\phi_o=0.125$: (a) $C_P=0.0$ mg/ml; (b) $C_P=2.8$ mg/ml; (c) $C_P=4.1$ mg/ml; (d) $C_P=8.0$ mg/ml. The symbols are (■) measurements made at 20 min; (○) 60 min, and (▲) 100 min.

tween particles. Separations equal to one particle diameter identify particles in contact. Figure 8 shows the distribution of N_b per particle as a function of polymer concentration for $\phi_o=0.125$. These results are typical for all of the initial volume fractions investigated. The initial bond number observed at the beginning of the compaction process decreases with increasing polymer concentration, reflecting the more open structure formed as the attractive interactions increase. At polymer concentrations above 4.1 mg/ml, more than 80% of particles are distributed in the range of $N_b=2-5$, which is substantially lower than in random close packing. Similar to changes in ϕ_{sed}, there is a distinct shift in the average bond number for the samples, depending on the polymer concentration. The change in N_b is greatest in the absence of polymer, where the distribution peak shifts from approximately six bonds per particle to approximately seven over a 1 h period. At $C_P=2.8$ mg/ml, the distribution peak exhibits a less pronounced change from approximately five bonds per particle to six. However, for $C_P=4.1$ and 8.0 mg/ml, the bond number distribution does not change significantly over the initial hour. A slight increase is observed for $C_P=4.1$ mg/ml at 100 min after forming the sediment, while the sample with the highest polymer concentration ($C_P=8.0$ mg/ml) does not appear to change at all.

An advantage of confocal microscopy is that the changes in bond number distributions can be characterized as a function of position inside the sediment layer. This enables the identification of regions that exhibit significant movement or collapse. Figure 9 shows images of the sediment layers reconstructed from the 3D coordinates of particles as a function of polymer concentration at $\phi_o=0.125$. The spheres are color-coded to indicate the number of bonds, as described in the figure caption. As expected from the behavior shown in Figs. 6 and 8, below $C_P=2.8$ mg/ml, the sediment has dense structure and exhibits significant rearrangements that lead to an overall increase in the bond number per particle. However, Figs. 9(a) and 9(b) demonstrate that there are no distinct patterns of compaction; instead, it appears to take place uniformly throughout the entire sediment volume. Above $C_P=4.1$ mg/ml, the sediment is more porous and has fewer bonds per particle. Nonetheless, the compaction again appears to occur uniformly in the sediment.

Finally, the bond angle distribution is calculated with particle triplets in the sediment volume. Triplets are identified when two particles separated by a distance r_3 ($2a \leqslant r_3 \leqslant 4a$, where $2a$ is particle diameter) have a common nearest neighbor. The inter particle distances (r_1, r_2, and r_3) are related to the bond angle (θ) between two adjacent sides by $\cos\theta=(r_1^2+r_2^2-r_3^2)/2r_1r_2$. The angles $\theta=60°$, 109.3°, and 120° originate from the equilateral triangle, tetrahedron, and isosceles triangle of particles, respectively. These represent stable, multiply bonded structures that are expected to form in glasses and gels with centrosymmetric particle interactions [38]. Although we cannot identify discrete rearrangements that underlie the compaction process in the sediment, in most cases, particles in the sediment adopt more stable configurations over time. Figure 10 shows the bond angle distributions with time for $\phi_o=0.125$ in the absence of nonadsorbing polymer and three increasing polymer concentrations. For $C_P=0$ and 2.8 mg/ml, two peaks emerge at 60° and 109° an hour after the initial sediment formation, corresponding to the development of multiply bonded structures. At polymer concentrations $C_P=4.1$ and 8.0 mg/ml, we cannot identify changes or specific peaks in the bond angle distribution within the noise of our experiment.

IV. DISCUSSION

As shown in this study, external fields such as gravity have a considerable effect on the ultimate structure of aggregating suspensions when compared to studies of aggregation

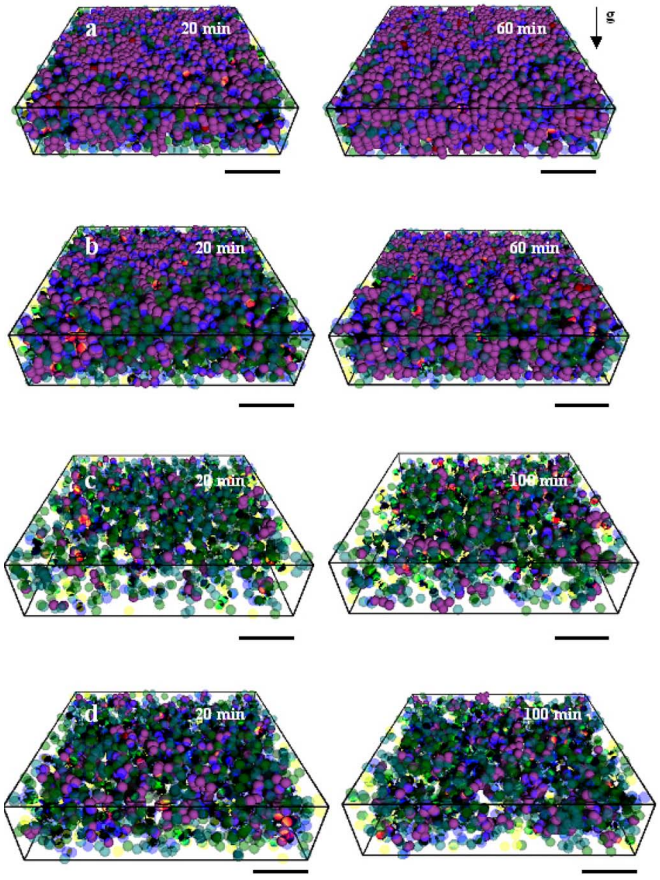

FIG. 9. (Color online) Visualizations of the structural evolution of sediments. (a) C_P=0.0 mg/ml; (b) C_P=2.8 mg/ml; (c) C_P =4.1 mg/ml; (d) C_P=8.0 mg/ml at ϕ_o=0.125. Particles are described with seven different colors, depending the number of bonds per particles. A white circle means that a particle has no bond. Yellow, green, cyan, and blue represent one to four bonds, respectively. A pink indicates five to nine bonds. A red means greater than ten bonds. Particles with fewer than five bonds are rendered translucently.

in the absence of sedimentation [4–9]. In the latter, the structure consists of growing flocs, which evolve into a tenuous, space-filling network. In the presence of gravity, relatively small changes in the initial volume fraction and attractive well depth lead to vastly different sediment structures as the competition between aggregation and sedimentation is altered. An especially important factor becomes the ability to form aggregates in the limited amount of time before particles are arrested as they reach the container bottom. Thus, the presediment structure, which depends strongly on polymer concentration and particle volume fraction, ultimately determines the sediment structure. In the following sections, we discuss the factors that govern presediment structure and its connection to the final sediment structure. We conclude by discussing the rearrangements and compaction in the sediments.

A. The effect of sticking probability and collision frequency on the presediment structure

The aggregation behavior during sedimentation depends on the sticking probability and collision frequency between particles. This accounts for the observation that the average cluster size is similar at higher volume fractions and lower polymer concentrations when compared to more dilute suspensions at higher C_P. When both ϕ_o and C_P are accounted for in Eqs. (4) and (5), $\langle \xi \rangle_m$ collapses onto a master curve, as shown in Fig. 3(b). The exponential dependence of $\langle \xi \rangle_m$ on C_P suggests that the Kramers time, which is the mean escape time $\tau = \tau_0 \exp(-U_{min}/kT)$ for a particle in an attractive well of magnitude U_{min}, plays a key role by governing the rate of bond ruptures due to hydrodynamic and gravitational stresses exerted on the growing aggregates. This is in qualitative agreement with simulations, which show that an increase in sticking probability leads to a faster increase in the average cluster size during settling [39].

A relationship similar to Eqs. (4) and (5) has been proposed to account for thermally activated barrier hopping processes in colloidal gels [40],

$$\tau/\tau_0 = Q \exp[4.2G(\phi)(C_p/C_p^*)(a/R_g)^{3/4}], \tag{9}$$

where Q is a preexponential factor, C_p^* is the polymer overlap concentration, and $G(\phi)$ is a function that empirically accounts for the volume fraction dependence and has a quadratic form. The increase in the barrier with increasing volume fraction is understood in terms of the increase in the number of bonds required to remove particles in a multiply bonded structure. Notably, the functional form of Eqs. (4) and (9) also describes the collapse time $t_{collapse}$ of gels in delayed sedimentation studies, reported by Kilfoil and coworkers [41]. They found that $t_{collapse}$ increases with C_P and ϕ by $t_{collapse} \sim \tau_o \exp[\beta(\phi)C_P]$, where $\beta(\phi)$ is a fitting parameter that accounts for the volume fraction dependence. Again, $t_{collapse}$ depends exponentially on the polymer concentration. The effect of volume fraction was described by empirical function $\beta(\phi)$, which was found to be independent of ϕ at $\phi \leqslant 0.1$ and to be linear function of volume fraction in the range of ϕ=0.1–0.2. Presumably, similar barrier hopping dynamics underlie the structural rearrangements that ultimately lead to gel collapse under gravitational stresses.

Several factors influence the volume fraction dependence. Under extremely dilute conditions, the decrease in the particle concentration leads to an increase in the mean distances between particles, therefore decreasing the rates of encounter between particles. Under such conditions, the lower collision frequency is inadequate to form aggregates in the limited time due to sedimentation. Similar results have been found in previous simulation studies [29,42,43]. For instance, González and co-workers studied the effect of volume fraction on colloidal aggregation in computer simulations as a function of the gravitational Peclet number Pe_g [29]. They found that an increasing particle concentration enhances the probability for forming aggregates. However, in the case of very dilute systems at high Pe_g, an enormous height of the suspension volume is required to increase the encounter rates. At higher concentrations, more collisions occur, but the net addition of particles to the growing aggregate depends again on the sticking probability.

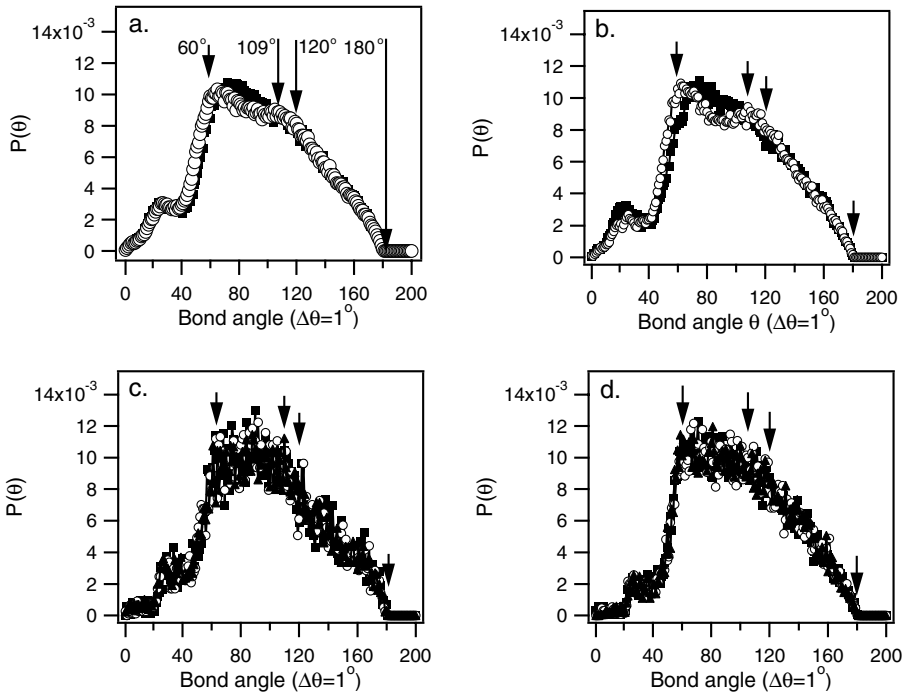

FIG. 10. Evolution of bond angle distribution in sediments at ϕ_o=0.125: (a) C_P=0.0 mg/ml; (b) C_P=2.8 mg/ml; (c) C_P=4.1 mg/ml; (d) C_P=8.0 mg/ml. The symbols are (■) measurements made at 20 min; (○) 60 min, and (▲) 100 min. The angles θ=60°, 109.3°, and 120°, originate from the equilateral triangle, tetrahedron, and isosceles triangle of particles, respectively. These represent stable, multiply bonded microstructures that are expected to form in colloidal glasses and gels with centrosymmetric particle interactions.

B. Relationship between the presediment and sediment structure

Our results highlight the strong correlation between the presediment and sediment structures, which are summarized in Fig. 11 as functions of C_P and ϕ_o. In the absence of nonadsorbing polymer (C_P=0 mg/ml), sediments form purely by deposition of particles. As the layer builds, the particles exhibit kinetic arrest that constrains Brownian motion due to the high volume fraction. As a result, the sediment layers are glassy or crystalline, depending on how quickly the sediment forms, and the magnitude of gravitational stresses compressing the sediment. This behavior is consistent with extensive studies of sedimenting hard sphere systems [44–46]. As the particle volume fraction increases, suspensions are observed to first undergo a disorder-order transition when the volume fraction exceeds ϕ_{sed}=0.495 and then form random glassy structures as the glass transition volume fraction is approached ($\phi_{sed} \approx 0.58$). Pusey and co-workers studied the effect of gravity on the structure of colloidal dispersions [46]. For dilute samples ($\phi \approx 0.25$) left for several weeks, crystals grew from the bottom of the cell due to the slow gravitational settling of particles.

In the presence of attractive interactions, sediments form by two distinct paths. At low nonadsorbing polymer concentrations, insufficient attractive forces restrict the size of aggregates in the presediment. Similar to hard-sphere deposition, single particles and small aggregates (mainly doublets) settle individually. However, the short-range attraction leads to the formation of bonds between particles in the sediment, causing a restriction in their motion that results in a structure with small voids. These structures form below C_{crit}, the polymer concentration that demarcates dense sediments from more open sediments in Table I. In contrast, at high polymer concentrations ($C_P > C_{crit}$), the strong attractive forces cause the rapid formation of large clusters. Aggregates grow by a sweeping mechanism [19,29], enhanced by the fact that clusters of different size sediment at different rates [47,48]. As large clusters arrive at the bottom of the container, they continue to pile up, forming the bond between particles in contact. They do not rearrange easily, leaving many large voids in the sediment.

Not surprisingly, there is a strong correlation between the formation of large aggregates in the presediment and the polymer concentration C_{crit} that marks the boundary between dense sediments and more open structures. The sediment

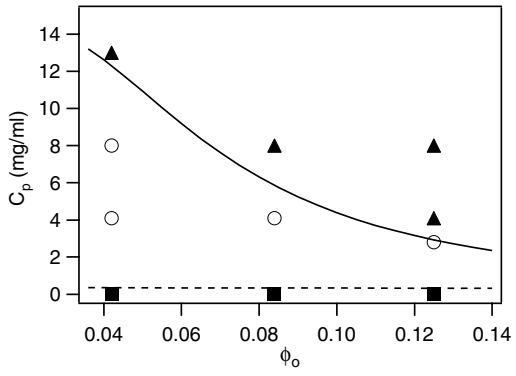

FIG. 11. The relationship between the presediment and sediment microstructure. Sediment structures are distinguished as the following: (■) glassy and partially crystalline layers with $\phi_{sed} \geq 0.517$; (○) dense sediments with $0.425 \leq \phi_{sed} \leq 0.508$; (▲) less dense sediments with $\phi_{sed} \leq 0.341$. See Table I for more details of the structure. The sediment volume fractions are for initial measurements made immediately after the formation of the initial sediment formation. The solid black line represents the critical polymer concentration (C_{crit}) defined by Eq. (4) for $\langle \xi \rangle_m / a$=4. The dashed line indicates $-U_{min}/kT$=1.

structure can be identified by the initial volume fraction and polymer concentration that results in the formation of aggregates larger than approximately $\langle \xi \rangle_m / a = 4$ before reaching the bottom of the container. Using Eq. (4), we plot C_P in Fig. 11 for values of ϕ_0 that satisfy this condition. Figure 11 shows that the transition from dense to less dense sediments based on the presediment structure is in excellent agreement with C_{crit}.

C. Longtime compaction of sediments

The density mismatch between particles and solvent leads to gravitational stresses in the sediment layers, which results in further compression. As demonstrated by the change in the sediment volume fraction (Table I), bond number distribution (Fig. 8) and bond angle distribution (Fig. 10), the degree of compaction depends strongly on the polymer concentration. For $C_P > C_{crit}$, gravity-driven compaction takes place slowly, if at all, due to the high bond strength, whereas in weakly attractive gels and glassy sediments ($0 \leqslant C_P < C_{crit}$), significant compaction occurs. The dependence on the attraction strength again reflects the typical lifetime of a depletion bond, as discussed earlier. It is interesting to note that the bond strength plays a much greater role in compaction than the structure of the sediment. Increasing polymer concentration leads to more free volume in the sediment and a greater number of weaker points, such as singly connected bonds, as indicated by the broader distribution of bond angles. Nonetheless, these more tenuous, but stronger sediments exhibit very little compaction.

Although the sediment layers are found to compact under gravity, we cannot directly identify individual rearrangements in the structure during this process. It appears that the compaction is occurring via extremely small rearrangements that are difficult to track over extended periods of time. Perhaps this is not surprising given the short range of the attraction induced by nonadsorbing polymer and the fact that the force is highest for particles in contact. Only small changes in separation between particles are required to form or break stress-bearing bonds.

V. CONCLUSIONS

In this work, we have investigated the effect of the sedimentation on colloidal aggregation. The experiments enabled us to track the development of structure from aggregation in solution to the formation of sediment layers. The nature of the growing structure during sedimentation suggests a dependence on the sticking probability of the colloid-colloid bonds. The functional form that described the growth of aggregates in the presediment is identical to recent theories of activated barrier hopping in attractive colloidal systems. Previously, this behavior was observed in the delayed sedimentation of colloidal gels. The early aggregation behavior determined the final structure of the suspension, and provides a means for controlling the porosity of the sediment through the void structure, and the aging properties of the sediment. Finally, we found that compaction and rearrangements in the sediment correlate strongly with the depth of attraction, but not with the sediment structure.

Several interesting questions remain for the aging stage where the mechanical properties of the sediment have to be considered. External forces and fields, including gravitation and shear deformation, lead to microstructural transitions that depend on the nature and strength of interparticle interactions and on the connectedness and topology of the gel. Characterizations of the microstructure and its response to perturbations enable us to understand and control the rheology of gels. In the silica sediments investigated here, however, it was impossible to directly track the structural deformation and small rearrangements that lead to compaction. A possible means to overcome this challenge is through the use optical or magnetic tweezers, which provide a tunable external force to probe the microscopic mechanical processes in colloidal glasses and gels [49,50].

ACKNOWLEDGMENTS

The authors thank K. Schweizer, M. Solomon, and R. Butera for helpful discussions. This research was supported by the National Science Foundation under Grant No. CTS-0238689.

[1] F. Pierce, A. Chakrabarti, D. Fry, and C. M. Sorensen, Langmuir **20**, 2498 (2004).
[2] M. D. Haw, M. Sievwright, W. C. K. Poon, and P. N. Pusey, Adv. Colloid Interface Sci. **62**, 1 (1995).
[3] R. G. Larson, *The Structure and Rheology of Complex Fluids* (Oxford University Press, New York, 1999).
[4] D. A. Weitz, J. S. Huang, M. Y. Lin, and J. Sung, Phys. Rev. Lett. **53**, 1657 (1984).
[5] D. A. Weitz, J. S. Huang, M. Y. Lin, and J. Sung, Phys. Rev. Lett. **54**, 1416 (1985).
[6] P. Dimon, S. K. Sinha, D. A. Weitz, C. R. Safinya, G. S. Smith, W. A. Varady, and H. M. Lindsay, Phys. Rev. Lett. **57**, 595 (1986).
[7] M. L. Broide and R. J. Cohen, Phys. Rev. Lett. **64**, 2026 (1990).
[8] M. Carpineti, F. Ferri, M. Giglio, E. Paganini, and U. Perini, Phys. Rev. A **42**, 7347 (1990).
[9] S. Stoll and E. Pefferkorn, J. Colloid Interface Sci. **152**, 247 (1992).
[10] D. A. Weitz and M. Oliveria, Phys. Rev. Lett. **52**, 1433 (1984).
[11] P. Meakin, Phys. Rev. Lett. **51**, 1119 (1983).
[12] M. Carpineti and M. Giglio, Phys. Rev. Lett. **68**, 3327 (1992).
[13] S. Feng and P. N. Sen, Phys. Rev. Lett. **52**, 216 (1984).
[14] W. Lee, A. Chan, J. A. Lewis, and P. V. Braun, Langmuir **20**, 5262 (2004).
[15] M. A. Bevan, J. A. Lewis, P. V. Braun, and P. Wiltzius, Langmuir **20**, 7045 (2004).
[16] A. van Blaaderen, R. Ruel, and P. Wiltzius, Nature **385**, 321

(1997).
[17] A. van Blaaderen and P. Wiltzius, Adv. Mater. (Weinheim, Ger.) **9**, 833 (1997).
[18] G. Odriozola, R. Leone, A. Moncho-Jorda, A. Schmitt, and R. Hidalgo-Alvarez, Physica A **335**, 35 (2004).
[19] A. E. González, Phys. Rev. Lett. **86**, 1243 (2001).
[20] C. Allain, M. Cloitre, and M. Wafra, Phys. Rev. Lett. **74**, 1478 (1995).
[21] R. Leone, G. Odriozola, L. Mussio, A. Schmitt, and R. Hidalgo-Alvarez, Eur. Phys. J. E **7**, 153 (2002).
[22] S. Manley, L. Cipelletti, V. Trappe, A. E. Bailey, R. J. Christianson, U. Gasser, V. Prasad, P. N. Segre, M. P. Doherty, S. Sankaran, A. L. Jankovsky, B. Shiley, J. Bowen, J. Eggers, C. Kurta, T. Lorik, and D. A. Weitz, Phys. Rev. Lett. **93**, 108302 (2004).
[23] L. Starrs, W. C. K. Poon, D. J. Hibberd, and M. M. Robins, J. Phys.: Condens. Matter **14**, 2485 (2002).
[24] S. Manley, J. M. Skotheim, L. Mahadevan, and D. A. Weitz, Phys. Rev. Lett. **94**, 218302 (2005).
[25] M. H. Lee, F. L. Beyer, and E. M. Furst, J. Colloid Interface Sci. **288**, 114 (2005).
[26] V. A. Tolpekin, M. H. G. Duits, D. van den Ende, and J. Mellema, Langmuir **20**, 2614 (2004).
[27] J. C. Crocker and D. G. Grier, J. Colloid Interface Sci. **179**, 298 (1996).
[28] P. Varadan and M. J. Solomon, J. Rheol. **47**(4), 943 (2003).
[29] A. E. González, G. Odriozola, and R. Leone, Eur. Phys. J. E **13**, 165 (2004).
[30] D. W. Schaefer, J. E. Martin, P. Wiltzius, and D. S. Cannell, Phys. Rev. Lett. **52**, 2371 (1984).
[31] F. Ferri, B. J. Frisken, and D. S. Cannell, Phys. Rev. Lett. **67**, 3626 (1991).
[32] H. F. van Garderen, W. H. Dokter, T. P. M. Beelen, R. A. van Santen, E. Pantos, M. A. J. Michels, and P. A. J. Hilbers, J. Chem. Phys. **102**(1), 480 (1995).
[33] H. Boukari, J. S. Lin, and M. T. Harris, J. Colloid Interface Sci. **194**, 311 (1997).
[34] H. F. van Garderen, E. Pantos, W. H. Dokter, T. P. M. Beelen, and R. A. van Santen, Modell. Simul. Mater. Sci. Eng. **2**, 295 (1994).
[35] P. Varadan and M. J. Solomon, Langmuir **19**, 509 (2003).
[36] J. P. Hansen and I. R. McDonald, *Theory of Simple Liquids* (Academic Press, San Diego, CA, 1990).
[37] S. A. Shah, S. Ramakrishnan, Y.-L. Chen, K. S. Schweizer, and C. F. Zukoski, Langmuir **19**, 5128 (2003).
[38] M. Hütter, J. Colloid Interface Sci. **231**, 337 (2000).
[39] G. Odriozola, R. Leone, A. Schmitt, A. Moncho-Jordá, and R. Hidalgo-Álvarez, Phys. Rev. E **67**, 031401 (2003).
[40] Y.-L. Chen, V. Kobelev, and K. S. Schweizer, Phys. Rev. E **71**, 041405 (2005).
[41] M. L. Kilfoil, E. E. Pashkovski, J. A. Masters, and D. A. Weitz, Philos. Trans. R. Soc. London, Ser. A **361**, 753 (2003).
[42] M. D. Haw, M. Sievwright, W. C. K. Poon, and P. N. Pusey, Adv. Colloid Interface Sci. **62**, 1 (1995).
[43] A. E. González, J. Phys.: Condens. Matter **14**, 2335 (2002).
[44] V. C. Martelozzo, A. B. Schofield, W. C. K. Poon, and P. N. Pusey, Phys. Rev. E **66**, 021408 (2002).
[45] Z. Cheng, W. B. Russel, and P. M. Chaikin, Nature **401**, 893 (1999).
[46] P. N. Pusey, W. van Megen, P. Bartlett, B. J. Ackerson, J. G. Rarity, and S. M. Underwood, Phys. Rev. Lett. **63**, 2753 (1989).
[47] W. C. K. Poon, and M. D. Haw, Adv. Colloid Interface Sci. **73**, 71 (1997).
[48] W. B. Russel, D. A. Saville, and W. R. Schowalter, *Colloidal Dispersions* (Cambridge University Press, Cambridge, 1991).
[49] A. Meyer, A. Marshall, B. G. Bush, and E. M. Furst, J. Rheol. **50**(1), 77 (2006).
[50] P. Habdas and E. R. Weeks, Curr. Opin. Colloid Interface Sci. **7**, 196 (2002).